catalysts

MDPI

Article

Constructing Active Sites on Self-Supporting $Ti_3C_2T_x$ (T = OH) Nanosheets for Enhanced Photocatalytic CO_2 Reduction into Alcohols

Shuqu Zhang, Man Zhang, Wuwan Xiong, Jianfei Long, Yong Xu, Lixia Yang and Weili Dai *

Key Laboratory of Jiangxi Province for Persistent Pollutants Control and Resources Recycle, Nanchang Hangkong University, Nanchang 330063, China
* Correspondence: wldai81@126.com or daiweili@nchu.edu.cn

Abstract: $Ti_3C_2T_x$ (T = OH) was first prepared from Ti_3AlC_2 by HF etching and applied into a photocatalytic CO_2 reduction. Then, the $Ti_3C_2T_x$ nanosheets present interbedded a self-supporting structure and extended interlayer spacing. Meanwhile, the $Ti_3C_2T_x$ nanosheets are decorated with abundant oxygen-containing functional groups in the process of etching, which not only serve as active sites but also show efficient charge migration and separation. Among $Ti_3C_2T_x$ materials prepared by etching for different times, $Ti_3C_2T_x$-36 (Etching time: 36 h) showed the best performance for photoreduction of CO_2 into alcohols (methanol and ethanol), giving total yield of 61 μmol g catal.$^{-1}$, which is 2.8 times than that of Ti_3AlC_2. Moreover, excellent cycling stability for CO_2 reduction is beneficial from the stable morphology and crystalline structure. This work provided novel sights into constructing surface active sites controllably.

Keywords: photocatalytic CO_2 reduction; active sites; controllable exfoliation; $Ti_3C_2T_x$

Citation: Zhang, S.; Zhang, M.; Xiong, W.; Long, J.; Xu, Y.; Yang, L.; Dai, W. Constructing Active Sites on Self-Supporting $Ti_3C_2T_x$ (T = OH) Nanosheets for Enhanced Photocatalytic CO_2 Reduction into Alcohols. *Catalysts* **2022**, *12*, 1594. https://doi.org/10.3390/catal12121594

Academic Editors: Gassan Hodaifa, Rafael Borja and Mha Albqmi

Received: 8 November 2022
Accepted: 4 December 2022
Published: 6 December 2022

1. Introduction

The continuous CO_2 emissions due to the depletion of fossil fuels have caused emerging problems in the environment and energy sectors [1]. Solar-driven CO_2 reduction that can produce various carbon fuels is considered a desirable strategy to resolve these problems [2]. Nevertheless, the perfect photocatalytic reduction of CO_2 process needs to meet the enhanced and broaden light absorption, abundant active sites and efficient charges separation [3]. At present, the researchers devote themselves improving the efficiency for photocatalytic CO_2 reduction towards the abovementioned objectives.

Two-dimensional semiconductors are valuable materials for photocatalytic applications because of their larger surface area and excellent electron mobility [4–7]. As a surface catalytic reaction, the performance of photocatalytic CO_2 reduction is also seriously determined by the reactive sites on the surface of photocatalysts [8]. Therefore, it is still urgent for constructing active sites on the surface of two-dimensional semiconductor photocatalysts to further enhance photocatalytic performance [9]. MXenes is formulated as $M_{n+1}X_nT_x$, in which M is a transition metal such as Ti, X is C or N, and T is a surface termination group such as -O or -OH [10]. They can be obtained by removing element A (mostly Al) from a ternary parent MAX phase through liquid exfoliation [11,12]. It was known that MXenes acted as a cocatalyst in photocatalytic CO_2 reduction due to its huge surface and excellent electronic conductivity [13]. Its huge surface provides the anchored sites for CO_2, and its excellent electronic conductivity is beneficial for migration of photogenerated electrons. However, there are still no reports about MXenes as separate photocatalyst in CO_2 reduction. As reported, the terminal oxygen-containing functional group on the MXenes surface could be redox-active [14]. Therefore, it is necessary to prepare MXenes nanosheets with a large surface area and explore the role of terminal functional groups on the performance of photocatalytic CO_2 reduction.

In this work, $Ti_3C_2T_X$ nanosheets were prepared by controllable etching, and firstly applicated into a photocatalytic CO_2 reduction. The $Ti_3C_2T_X$ nanosheets were decorated with different types of the oxygen-containing functional group. The interbedded self-supporting structure of layered $Ti_3C_2T_X$ not only exposed more active sites and preserved the stability of morphology and crystalline structure, but also benefitted for charge migration and separation. Eventually, $Ti_3C_2T_X$ nanosheets delivered excellent performance and stability for photocatalytic CO_2 reduction.

2. Results and Discussion

The XRD pattern was shown to investigate the stacking property and layered structure (Figure 1a). Diffraction peaks of $Ti_3C_2T_x$ correspond to JCPDS No. 52-0875. Stacking peak {002} shifts to a lower angle compared with Ti_3AlC_2, indicating extended interlayer spacing in Figure 1b [15]. $Ti_3C_2T_x$-36 shows the largest specific surface area among all the photocatalysts samples, which means that the $Ti_3C_2T_x$-36 holds the largest interlayer spacing, showing the lowest {002} peak intensity. Raman spectra of different samples was shown in Figure S1. The enhanced peak intensity at 203 cm^{-1} suggests powerful Ti-C vibration in $Ti_3C_2T_x$ [16]. The peak at 273 cm^{-1} belonging to Ti-Al vibration in Ti_3AlC_2 disappeared after etching. The enhanced Ti-C vibration and disappeared Ti-Al vibration suggest the removal of the Al layer. "Eg vibration" corresponds to out-of-plane vibration of Raman scattering for two-dimensional nanosheets. Eg vibration presents enhanced Raman scattering at 628 cm^{-1} for decoration of -OH groups on the terminated C atom of Ti_3C_2 [17]. All indicate successful formation of $Ti_3C_2T_x$ and decoration of oxygen-containing functional groups on it.

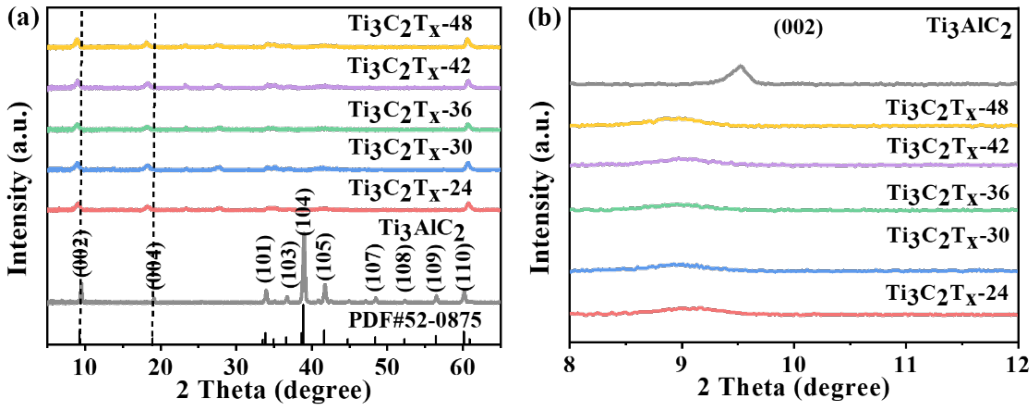

Figure 1. (**a**) XRD pattern and (**b**) (002) peak of Ti_3AlC_2, $Ti_3C_2T_x$-y nanosheets (y = 24, 30, 36, 42 and 48).

Figure 2 showed SEM images for $Ti_3C_2T_x$ samples with different etching time (24 h, 30 h, 36 h, 42 h and 48 h). $Ti_3C_2T_x$ samples show the obvious morphological features of layered structure with broadened interlayer spacing. It can be observed that $Ti_3C_2T_x$-36 shows uniform layers and a smooth surface. However, the $Ti_3C_2T_x$-42 and $Ti_3C_2T_x$-48 tended to aggregate and stack again with the increasing etching time. It is well accepted that the catalysis generally occurs on the active sites, while the active sites mostly exist in the edges, unsaturated steps, terraces, kinks, and/or corner atoms for layered structures [3,18].

The catalysts' surface holds a spot of active sites. The stacking, layered structure may cause the less active sites' exposure. $Ti_3C_2T_x$-36 shows a uniform layered structure (Figure S2a). Elemental mapping spectra presented Ti, C and O elements in Figure S2b,d. Oxygen-containing functional groups are decorated on the surface. The atomic structure of $Ti_3C_2T_x$ nanosheets is shown in Figure S2e. The side view for $Ti_3C_2T_x$ nanosheets shows a broadening layered structure (Figure S2f). TG analysis was conducted to inspect thermostability in Figure S3. $Ti_3C_2T_x$ nanosheets decorated with oxygen-containing functional groups shows the interbedded self-supporting structure, which also preserves morphological stability. Specifically, $Ti_3C_2T_x$-36 showed the best thermostability among all $Ti_3C_2T_x$

samples. The specific area of Ti_3AlC_2, $Ti_3C_2T_x$-24, $Ti_3C_2T_x$-30, $Ti_3C_2T_x$-36, $Ti_3C_2T_x$-42 and $Ti_3C_2T_x$-48 nanosheets are 0.56, 2.49, 3.27, 3.52, 2.97 and 1.41 m^2/g, respectively. $Ti_3C_2T_x$ shows a larger specific surface area compared with Ti_3AlC_2 form Nitrogen adsorption–desorption isotherms (Figure S4). $Ti_3C_2T_x$-36 holds the highest specific surface area and pore volume. The extended interlayer spacing means more surface is exposed and the stacking structure becomes open architecture. It is reported that the open architecture is beneficial for migration and diffusion of photogenerated carriers [19]. $Ti_3C_2T_x$-42 and $Ti_3C_2T_x$-48, with prolonged etching times, present the smaller specific surface area due to the stacking layers, which is in accord with the morphological features from Figure 1.

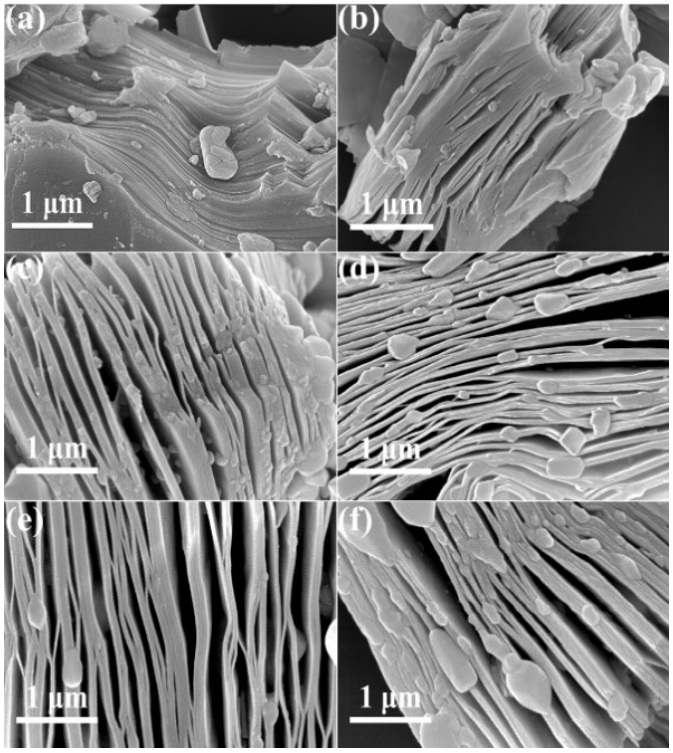

Figure 2. SEM images of (**a**) Ti_3AlC_2, (**b**) $Ti_3C_2T_X$-24, (**c**) $Ti_3C_2T_X$-30, (**d**) $Ti_3C_2T_X$-36, (**e**) $Ti_3C_2T_X$-42 and (**f**) $Ti_3C_2T_X$-48.

It is necessary to investigate the photoelectric property and identify performance of carrier separation. $Ti_3C_2T_x$ shows excellent UV-*vis* absorption ability (Figure S5a). The bandgap structure is not changed even though $Ti_3C_2T_x$ nanosheets are decorated with different oxygen-containing functional groups. The bandgap of $Ti_3C_2T_x$-24, $Ti_3C_2T_x$-30, $Ti_3C_2T_x$-36, $Ti_3C_2T_x$-42 and $Ti_3C_2T_x$-48 samples is 2.21, 2.14, 2.22, 2.38, 2.26 V, respectively, from the Kubelka–Munk function $(Ah\upsilon)^2$ vs. light energy ($h\upsilon$) in Figure S5b. The flat band potential (FB) of $Ti_3C_2T_x$ is −0.53 V vs. SCE by Mott-Schottky spectra in Figure S5c. The conduction band (CB) can be calculated as −0.39 V vs. NHE by the following equation:

$$E_{vs.\ NHE} = E_{FB} + E^0 + 0.059pH. \quad (1)$$

The valence band (VB) of $Ti_3C_2T_x$ is 1.82, 1.75, 1.83, 1.99, and 1.87 V vs. NHE (pH = 7) by the following equation:

$$(E_{VB} = E_{CB} + Eg) \quad (2)$$

It is reported that the oxidation potential is 0.82 V (vs. NHE, pH = 7) [20–22]. $Ti_3C_2T_x$ holds the ability to oxidize H_2O to provide H protons for a CO_2 reduction rection.

$Ti_3C_2T_x$-36 shows highest photocurrent, indicating efficient separation and transportation of photoinduced charge carriers (Figure 3a). In addition, $Ti_3C_2T_x$-36 shows a much

smaller radius from electrochemical impedance spectroscopy (EIS) spectra (Figure 3b), demonstrating fast interfacial charge transfer. The efficient separation of photogenerated carriers and longer fluorescence (PL) lifetime imply that $Ti_3C_2T_x$-36 showed the best carrier generation and separation capability (Figure 3c,d). The enhanced photoelectric property is due to extended interlayer spacing and more introduced active sites.

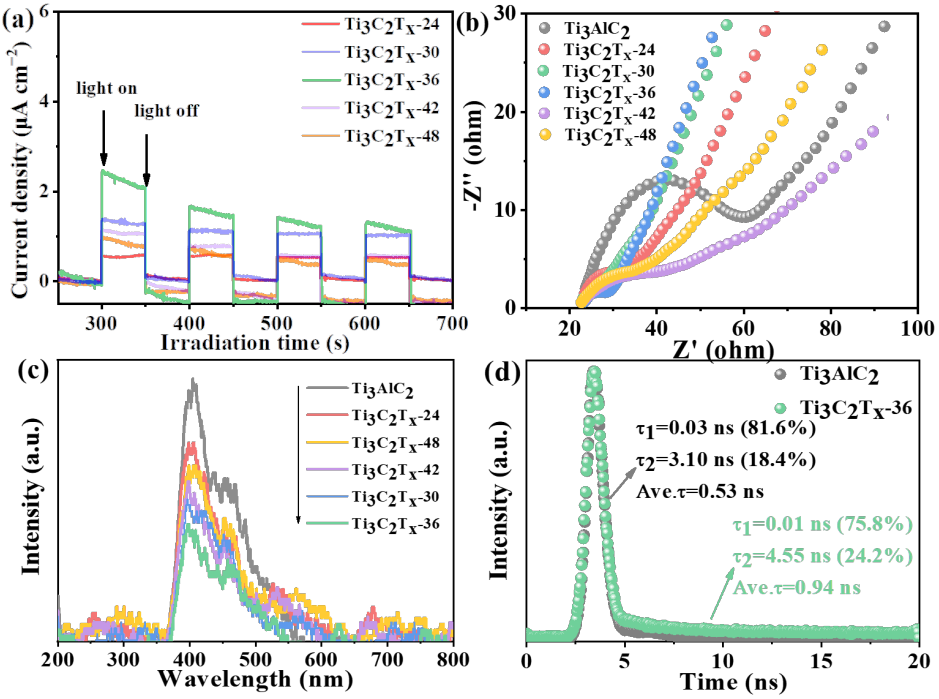

Figure 3. (**a**) Transient photocurrent responses, (**b**) EIS Nyquist plots, (**c**) PL spectra and (**d**) TRPL decay spectra of prepared photocatalysts.

The $Ti_3C_2T_x$ showed the better photoelectric property, therefore, it is needed to inspect the surface property of $Ti_3C_2T_x$. FTIR spectra was conducted to analyze the functional groups in Figure 4a. A length of 775–1237 cm^{-1} corresponds to various Ti-O vibrational modes [23]. A length of 1607 and 1631 cm^{-1} absorbs O vibration. A length of 2345 and 2372 cm^{-1} belongs to -OH groups vibration. A length of 3396 cm^{-1} corresponds to absorbed H_2O. The $Ti_3C_2T_x$ nanosheets were prepared by HF etching, therefore, there are few -F function groups linked with the C atom after Al removal (Figure S6a,b). The abundant oxygen-containing functional groups (i.e., -O, -OH) are decorated on the terminus of Ti_3C_2 after etching exfoliation from XPS measurement (Figure S6c). The binding energy at 527.15, 528.45 and 530.35 eV absorb O, -OH/Ox and H_2O, respectively [24]. The high-resolution XPS spectra of O 1s for the samples are analyzed to figure out the crucial oxygen-containing functional group in Figure 4b. The analysis results are listed in Figure 4c. The atomic O contents for $Ti_3C_2T_x$-24, $Ti_3C_2T_x$-30, $Ti_3C_2T_x$-36, $Ti_3C_2T_x$-42 and $Ti_3C_2T_x$-48 samples are 15.96%, 16.27%, 16.98%, 15.46% and 15.92%, respectively. $Ti_3C_2T_x$-36 shows the highest atomic O content because more oxygen-containing groups are decorated on a larger surface area. The stacking layers for $Ti_3C_2T_x$-42 and $Ti_3C_2T_x$-48 lead to the smaller O content. In $Ti_3C_2T_x$-36, the -OH/Ox and H_2O showed the highest content compared with other photocatalyst samples from the integral area of the corresponding peak, which means these two oxygen-containing groups play a crucial role for better photoelectric properties. As result, $Ti_3C_2T_x$-36 shows better dispersion from the morphological features of the layered structure in Figure S2g, which is due to the wider interlayer spacing for the decoration of -OH and -F functional groups. The selected area electron diffraction (SAED) pattern of $Ti_3C_2T_x$-36 suggests preservation of hexagonal basal structure derived from

Ti_3AlC_2 (Figure S2h) [25]. It was reported that this oxygen-containing functional group on the $Ti_3C_2T_x$ terminal could be redox-active, serving as adsorption active sites for CO_2 [26].

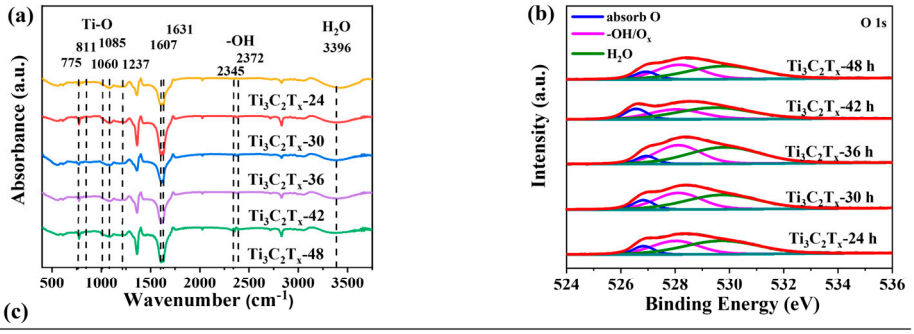

(c)

Samples	Atomic Content of O (%)	Content of –absorb O		Content of –OH/O_x		Content of H_2O	
		Binding Energy (eV)	Area	Binding Energy (eV)	Area	Binding Energy (eV)	Area
$Ti_3C_2T_x$-24	15.86	526.84	2386	528.02	8958	529.70	1,4042
$Ti_3C_2T_x$-30	16.26	526.86	2719	528.15	1,0721	529.78	1,4770
$Ti_3C_2T_x$-36	16.89	526.93	2264	528.11	1,1731	529.81	1,6733
$Ti_3C_2T_x$-42	13.33	526.59	3260	528.07	7431	529.50	1,2313
$Ti_3C_2T_x$-48	15.66	526.96	2336	528.18	9512	529.85	1,3571

Figure 4. (**a**) FTIR spectra, (**b**) High-resolution XPS spectra of O 1s, (**c**) Table of different O group comparison of $Ti_3C_2T_X$-24, $Ti_3C_2T_X$-30, $Ti_3C_2T_X$-36, $Ti_3C_2T_X$-42 and $Ti_3C_2T_X$-48.

The photocatalytic CO_2 reduction was proceeded to evaluate photocatalytic performance for photocatalysts. The products of photocatalytic CO_2 reduction are methanol and ethanol, and $Ti_3C_2T_x$ samples show enhanced photocatalytic performance with increasing irradiation time (Figure 5a,b). The produced rate for methanol and ethanol over Ti_3AlC_2 is 12.9 μmol g catal.$^{-1}$ and 8.7 μmol g catal.$^{-1}$. Among all samples, $Ti_3C_2T_x$-36 gives best methanol and ethanol yields, 38.1 μmol g catal.$^{-1}$ and 22.9 μmol g catal.$^{-1}$ after 4 h irradiation, respectively. The total yield for $Ti_3C_2T_x$-36 is 2.8 times than that of Ti_3AlC_2. The methanol and ethanol yields after 4 h irradiation of $Ti_3C_2T_x$-24, $Ti_3C_2T_x$-30, $Ti_3C_2T_x$-42 and $Ti_3C_2T_x$-48 are 19.34 and 17.7, 30.99 and 17.05, 28.85 and 18.11 and 19.1 and 14.34 μmol g catal.$^{-1}$, respectively. It is noted that $Ti_3C_2T_x$-42 and $Ti_3C_2T_x$-48 with less O contents show poorer photocatalytic performance of CO_2 reduction due to the restacking layers. The oxygen-containing content shows a positive correlation with production yields (Figures 4c and 5a,b). Table S1 showed the comparison of photocatalytic activity for CO_2 reduction (products: methanol and ethanol) by some photocatalyst systems. The enhanced performance for CO_2 reduction is due to more active sites constructed on $Ti_3C_2T_x$ surface and efficient carrier separation. $^{13}CO_2$ was employed to replace $^{12}CO_2$ to confirm carbon source of the produced methanol and ethanol with the corresponding MS spectra shown in Figure 5c,d. The intense signals of m/z = 33 and m/z = 48 are assigned to $^{13}CH_3OH$ and $^{13}C_2H_5OH$, respectively. The nearby peaks belong to the fragment peaks. It verifies that CO_2 acts as the only carbon source of value-added alcohols over the $Ti_3C_2T_x$ photocatalyst. To further prove the water oxidation, O_2 amounts were detected during photocatalytic CO_2 reduction over $Ti_3C_2T_x$-36. The calibration curves of the relationships between peak area and O_2 volume was shown in Figure S7. The O_2 yield with 2, 5, 8, 13 μmol g catal.$^{-1}$ is increased during CO_2 reduction over $Ti_3C_2T_x$-36 in 4 h in Figure S8. It is true that self-supporting Ti_3C_2Tx nanosheets with constructed active sites could act as an efficient photocatalyst for CO_2 reduction and H_2O oxidation. The cycling stability of CO_2 reduction over $Ti_3C_2T_x$-36 was inspected in Figure 5e. The methanol and ethanol performance over $Ti_3C_2T_x$-36 in five cycles are 38.06 and 22.85, 32.1 and 28.64, 32.61 and 27.96, 31.5 and 27.52 and 30.49 and 27.42 μmol g catal.$^{-1}$, respectively. The performance over $Ti_3C_2T_x$-36 represents little decrease after five cycling runs, but crystal structure does not change (Figure 5f).

Interbedded self-supporting structures are responsible for excellent photocatalytic activity and stable morphology structure.

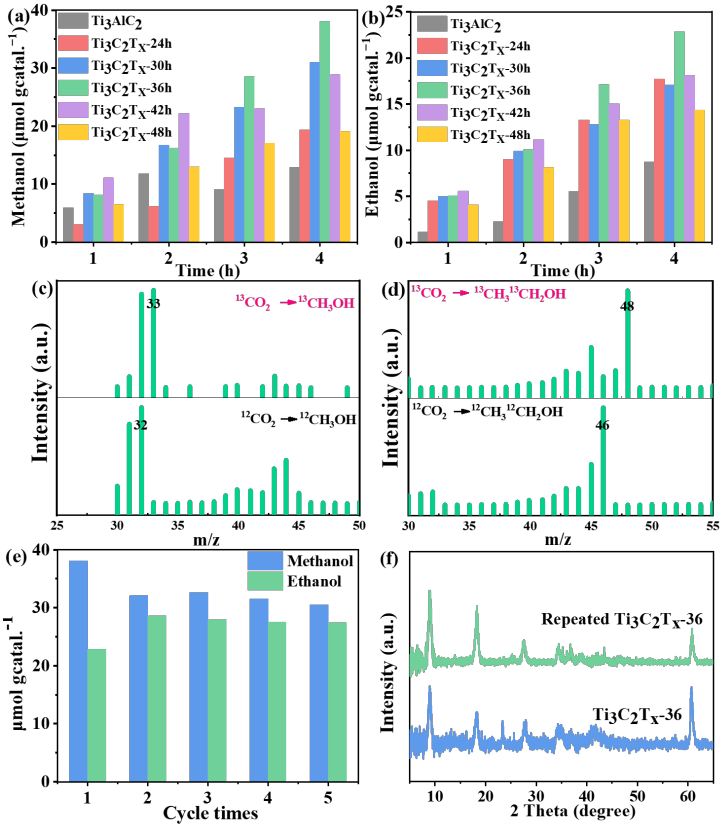

Figure 5. Yields of (**a**) methanol and (**b**) ethanol from photocatalytic CO_2 reduction under visible light. GC-MS spectra of (**c**) $^{13}CH_3OH$ and (**d**) $^{13}C_2H_5OH$ using $^{13}CO_2$ and $^{12}CO_2$ as the source of CO_2. (**e**) Cycling runs for CO_2 reduction over $Ti_3C_2T_x$-36. (**f**) XRD patterns of fresh and repeated $Ti_3C_2T_x$-36.

3. Materials and Methods

3.1. Preparation Methods

Ti_3AlC_2 powder (1 g) was dispersed in HF solution (10 mL) and vigorously stirred for different times at room temperature. The obtained powder was washed with deionized water until pH = 6, collected by centrifugation at 8000 rpm for 5 min and dried in the vacuum oven at 60 °C for 12 h. A series of $Ti_3C_2T_x$ were labeled as $Ti_3C_2T_x$-y (y = 24 h, 30 h, 36 h, 42 h and 48 h).

3.2. Materials Characterization

Crystal structure was analyzed by X-ray diffractometer with Cu Kα radiation (Bruker AXS-D8, Karlsruhe, Germany). Raman spectra of the samples were measured by Raman spectrophotometer (Horiba JY LabRAM HR800, Paris, France). Scanning electron microscope (SEM) images were obtained by Nova NanoSEM 450, Hillsboro, IL, USA, and transmission electron microscope (TEM) analyses were conducted with JEOL, JEM−2100F (HR, Tokyo, Japan). Specific surface area and pore property were collected by TriStar II 3020, Atlanta, GA, USA. Thermogravimetric (TG) analysis was obtained from SDT Q600 (TA Instruments, New Castle, DE, USA). Fourier transform infrared spectroscopy (FTIR) were conducted by Bruker VERTEX 70 (Bruker, Karlsruhe, Germany). X-ray photoelectron spectroscopy (XPS) was performed VG Escalab 250, Waltham, MA, USA spectrometer equipped with an Al anode. UV-*vis* diffuse reflectance spectra (DRS) were proceeded by Shimadzu UV-2450 (Tokyo, Japan) spectrophotometer. The photoluminescence (PL)

spectra were measured to inspect charge recombination (F7000, Hitachi, Tokyo, Japan). A time-resolved fluorescence spectrofluorometer was used from Edinburgh, FS5.

3.3. Photoelectrochemical Measurements

Transient photocurrent response, electrochemical impedance spectroscopy and Mott–Schottky curves were carried out on the electrochemical workstation (CHI760E, Shanghai, China) in a standard three-electrode system with the Pt mesh as the counter electrode, the Saturated Calomel Electrode as the reference electrode, and the sample loaded electrodes as the working electrode in 0.1 M Na_2SO_4 aqueous solution (electrolyte solution) at room temperature. The distance between the counter electrode and the working electrode is 2 cm. Indium tin oxide (ITO) with a 1.0 cm × 1.0 cm area photocatalyst was used as the working electrode. The photocurrent measurement of the photocatalyst is measured by several switching cycles of light irradiated by a 300 W xenon lamp (using a 420 nm cut off filter).

3.4. Photocatalytic Reaction

The assessment for photocatalytic performance of CO_2 reduction as follows: 30 mg photocatalyst was dispersed in 30 mL deionized water and put into the reactor. The reactor was vacuumized. The saturated solution was obtained after admission with CO_2 (50 mL/min, 0.5 h). The reaction temperature was controlled at 4 °C. With the increasing irradiation time (light source: 300 W xenon lamp with a 420 nm cut offfilter, Perfect-Light, Beijing, China), the liquid reduction products were analyzed by gas chromatograph (GC7920-TF2A) equipped with a flame ionized detector (FID) and SE-54 capillary column. The isotope-labeled photocatalytic CO_2 reduction tests were performed by replacing $^{12}CO_2$ with $^{13}CO_2$ gas, while keeping the other reaction conditions unaltered. The obtained mixed gas was analyzed by gas chromatography-mass spectrometry (GC Model 6890 N/MS Model 5973, Agilent Technologies, Palo Alto, CA, USA).

4. Conclusions

In this work, $Ti_3C_2T_X$ with abundant oxygen-containing functional groups was successfully prepared and applicated into photocatalytic CO_2 reduction under visible light. The controllable content of oxygen-containing functional groups was achieved by tuning etching times as shown by the TG and XPS analysis. The exfoliation by extending the interlayer spacing exposed more active sites for generating more photo-induced carriers. The decorated oxygen-containing functional groups was beneficial for the charge migration and separation. The result was that the $Ti_3C_2T_X$-36 showed the best performance for photocatalytic CO_2 reduction (alcohols over production rate: 61 μmol g catal.$^{-1}$), which is 2.8 time than that of Ti_3AlC_2. The interbedded self-supporting structure of layered $Ti_3C_2T_X$ after successful exfoliation showed excellent stability of morphological structure, resulting in cycling stability for CO_2 reduction.

Supplementary Materials: The following supporting information can be downloaded at: https://www.mdpi.com/article/10.3390/catal12121594/s1, Figure S1. Raman spectra of Ti_3AlC_2, $Ti_3C_2T_x$-y nanosheets (y= 24, 30, 36, 42 and 48); Figure S2. SEM image of (a) $Ti_3C_2T_x$-36, (b-d) elemental mappings of (a). (e) Atomic structure of $Ti_3C_2T_x$, (f) STEM image, (g) TEM image and (h) selected area electron diffraction (SAED) pattern of $Ti_3C_2T_x$-36; Figure S3. TG analysis of (a) Ti_3AlC_2, (b) $Ti_3C_2T_X$-24, (c) $Ti_3C_2T_X$-30, (d) $Ti_3C_2T_X$-36, (e) $Ti_3C_2T_X$-42 and (f) $Ti_3C_2T_X$-48; Figure S4. (a) Nitrogen adsorption−desorption isotherms, (b) corresponding pore size distribution curves, and (c) information contrast of BET surface area, pore size and pore volume of $Ti_3C_2T_X$ with different etching times; Figure S5. (a) UV-vis absorption spectra, (b) Plots of transformed Kubelka–Munk function $(Ahv)^2$ *vs* light energy (hv) and (c) Mott-Schottky spectra of $Ti_3C_2T_X$-24, $Ti_3C_2T_X$-30, $Ti_3C_2T_X$-36, $Ti_3C_2T_X$-42, $Ti_3C_2T_X$-48; Figure S6. High-resolution XPS spectra of (a) Ti 2p, (b) C 1s and (c) O 1s over $Ti_3C_2T_X$-36; Figure S7. Calibration curves of the relationships between peak area and O_2 volume; Figure S8. O_2 evolution during photocatalytic CO_2 reduction over $Ti_3C_2T_x$-36; Table S1. The

comparison of photocatalytic activity for CO_2 reduction (products: methanol and ethanol) by some photocatalyst systems [27–36].

Author Contributions: Conceptualization, S.Z.; Methodology, M.Z.; Methodology, W.X.; Formal analysis, J.L.; Investigation, Y.X.; Supervision, L.Y.; Writing—review and editing, W.D. All authors have read and agreed to the published version of the manuscript.

Funding: This work was financially supported by the National Natural Science Foundation of China (Grants 51908269, 52262037, 22006064, 52072165).

Data Availability Statement: In this manuscript, our characterizations were SEM, XRD, TEM, BET, and UV-*vis*. All data have been reported as the images.

Conflicts of Interest: The authors declare no conflict of interest.

References

1. Zhou, N.; Khanna, N.; Feng, W.; Ke, J.; Levine, M. Scenarios of energy efficiency and CO_2 emissions reduction potential in the buildings sector in China to year 2050. *Nat. Energy* **2018**, *3*, 978–984. [CrossRef]
2. He, J.; Janáky, C. Recent advances in solar-driven carbon dioxide conversion: Expectations versus reality. *ACS Energy Lett.* **2020**, *5*, 1996–2014. [CrossRef] [PubMed]
3. Luo, J.; Zhang, S.; Sun, M.; Yang, L.; Luo, S.; Crittenden, J. A critical review on energy conversion and environmental remediation of photocatalysts with remodeling crystal lattice, surface, and interface. *ACS Nano* **2019**, *13*, 9811–9840. [CrossRef]
4. Dai, W.; Yu, J.; Luo, S.; Hu, X.; Yang, L.; Zhang, S.; Li, B.; Luo, X.; Zou, J. WS_2 quantum dots seeding in Bi_2S_3 nanotubes: A novel Vis-NIR light sensitive photocatalyst with low-resistance junction interface for CO_2 reduction. *Chem. Eng. J.* **2020**, *389*, 123430. [CrossRef]
5. Dai, W.; Xiong, W.; Yu, J.; Zhang, S.; Li, B.; Yang, L.; Wang, T.; Luo, X.; Zou, J.; Luo, S. Bi_2MoO_6 Quantum Dots in Situ Grown on Reduced Graphene Oxide Layers: A Novel Electron-Rich Interface for Efficient CO_2 Reduction. *ACS Appl. Mater. Interfaces* **2020**, *12*, 25861–25874. [CrossRef] [PubMed]
6. Dai, W.; Long, J.; Yang, L.; Zhang, S.; Xu, Y.; Luo, X.; Zou, J.; Luo, S. Oxygen migration triggering molybdenum exposure in oxygen vacancy-rich ultra-thin Bi_2MoO_6 nanoflakes: Dual binding sites governing selective CO_2 reduction into liquid hydrocarbons. *J. Energy Chem.* **2021**, *61*, 281–289. [CrossRef]
7. Zhang, S.; Si, Y.; Li, B.; Yang, L.; Dai, W.; Luo, S. Atomic-Level and Modulated Interfaces of Photocatalyst Heterostructure Constructed by External Defect-Induced Strategy: A Critical Review. *Small* **2021**, *17*, 2004980. [CrossRef]
8. Habisreutinger, S.; Schmidt-Mende, L.; Stolarczyk, J. Photocatalytic reduction of CO_2 on TiO_2 and other semiconductors. *Angew. Chem. Int. Ed.* **2013**, *52*, 7372–7408. [CrossRef]
9. Liu, L.; Wang, S.; Huang, H.; Zhang, Y.; Ma, T. Surface sites engineering on semiconductors to boost photocatalytic CO_2 reduction. *Nano Energy* **2020**, *75*, 104959. [CrossRef]
10. Xiu, L.; Wang, Z.; Yu, M.; Wu, X.; Qiu, J. Aggregation-resistant 3D MXene-based architecture as efficient bifunctional electrocatalyst for overall water splitting. *ACS Nano* **2018**, *12*, 8017–8028. [CrossRef]
11. Li, T.; Yao, L.; Liu, Q.; Gu, J.; Luo, R.; Li, J.; Yan, X.; Wang, W.; Liu, P.; Chen, B.; et al. Fluorine-Free Synthesis of High-Purity $Ti_3C_2T_x$ (T = OH, O) via Alkali Treatment. *Angew. Chem. Int. Edit.* **2018**, *57*, 6115–6119. [CrossRef] [PubMed]
12. Natu, V.; Pai, R.; Sokol, M.; Carey, M.; Kalra, V.; Barsoum, M. 2D $Ti_3C_2T_z$ MXene synthesized by water-free etching of Ti_3AlC_2 in polar organic solvents. *Chem* **2020**, *6*, 616–630. [CrossRef]
13. He, F.; Zhu, B.; Cheng, B.; Yu, J.; Ho, W.; Macyk, W. 2D/2D/0D $TiO_2/C_3N_4/Ti_3C_2$ MXene composite S-scheme photocatalyst with enhanced CO_2 reduction activity. *Appl. Catal B-Environ.* **2020**, *272*, 119006. [CrossRef]
14. Lukatskaya, M.; Kota, S.; Lin, Z.; Zhao, M.-Q.; Shpigel, N.; Levi, M.; Halim, J.; Taberna, P.-L.; Barsoum, M.; Simon, P.; et al. Ultra-high-rate pseudocapacitive energy storage in two-dimensional transition metal carbides. *Nat. Energy* **2017**, *2*, 17105. [CrossRef]
15. Overbury, S.; Kolesnikov, A.; Brown, G.; Zhang, Z.; Nair, G.; Sacci, R.; Lotfi, R.; Duin, A.; Naguib, M. Complexity of intercalation in MXenes: Destabilization of urea by two-dimensional titanium carbide. *J. Am. Chem. Soc.* **2018**, *140*, 10305–10314. [CrossRef] [PubMed]
16. Li, M.; Han, M.; Zhou, J.; Deng, Q.; Zhou, X.; Xue, J.; Du, S.; Yin, X.; Huang, Q. Novel Scale-Like Structures of Graphite/TiC/Ti_3C_2 Hybrids for Electromagnetic Absorption. *Adv. Electron. Mater.* **2018**, *4*, 1700617. [CrossRef]
17. Sarycheva, A.; Makaryan, T.; Maleski, K.; Satheeshkumar, E.; Melikyan, A.; Minassian, H.; Yoshimura, M.; Gogotsi, Y. Two-dimensional titanium carbide (MXene) as surface-enhanced Raman scattering substrate. *J. Phys. Chem. C* **2017**, *121*, 19983–19988. [CrossRef]
18. Sun, Y.; Gao, S.; Lei, F.; Xie, Y. Atomically-thin two-dimensional sheets for understanding active sites in catalysis. *Chem. Soc. Rev.* **2015**, *44*, 623–636. [CrossRef]
19. Han, C.; Chen, Z.; Zhang, N.; Colmenares, J.; Xu, Y. Hierarchically CdS decorated 1D ZnO nanorods-2D graphene hybrids: Low temperature synthesis and enhanced photocatalytic performance. *Adv. Funct. Mater.* **2015**, *25*, 221–229. [CrossRef]

20. Ran, J.; Jaroniec, M.; Qiao, S. Cocatalysts in Semiconductor-based Photocatalytic CO_2 Reduction: Achievements, Challenges, and Opportunities. *Adv. Mater.* **2018**, *30*, 1704649. [CrossRef]
21. Li, Y.; Fan, S.; Tan, R.; Yao, H.; Peng, Y.; Liu, Q.; Li, Z. Selective Photocatalytic Reduction of CO_2 to CH_4 Modulated by Chloride Modification on Bi_2WO_6 Nanosheets. *ACS Appl. Mater. Interfaces* **2020**, *12*, 54507–54516. [CrossRef] [PubMed]
22. Zhang, S.; Xiong, W.; Long, J.; Si, Y.; Xu, Y.; Yang, L.; Zou, J.; Dai, W.; Luo, X.; Luo, S. High-throughput lateral and basal interface in CeO_2@$Ti_3C_2T_X$: Reverse and synergistic migration of carrier for enhanced photocatalytic CO_2 reduction. *J. Colloid Interfaces Sci.* **2022**, *615*, 716–724. [CrossRef] [PubMed]
23. Khan, A.; Tahir, M.; Zakaria, Z. Synergistic effect of anatase/rutile TiO_2 with exfoliated Ti_3C_2TR MXene multilayers composite for enhanced CO_2 photoreduction via dry and bi-reforming of methane under UV–visible light. *J. Environ. Chem. Eng.* **2021**, *9*, 105244. [CrossRef]
24. Kuang, P.; He, M.; Zhu, B.; Yu, J.; Fan, K.; Jaroniec, M. 0D/2D NiS_2/V-MXene composite for electrocatalytic H_2 evolution. *J. Catal.* **2019**, *375*, 8–20. [CrossRef]
25. He, P.; Cao, M.-S.; Shu, J.-C.; Cai, Y.; Wang, X.-X.; Zhao, Q.-L.; Yuan, J. Atomic layer tailoring titanium carbide MXene to tune transport and polarization for utilization of electromagnetic energy beyond solar and chemical energy. *ACS Appl. Mater. Interfaces* **2019**, *11*, 12535–12543. [CrossRef]
26. Li, W.; Jin, L.; Gao, F.; Wan, H.; Pu, Y.; Wei, X.; Chen, C.; Zou, W.; Zhu, C.; Dong, L. Advantageous roles of phosphate decorated octahedral CeO_2{111}/g-C_3N_4 in boosting photocatalytic CO_2 reduction: Charge transfer bridge and Lewis basic site. *Appl. Catal. B-Environ.* **2021**, *294*, 120257. [CrossRef]
27. Becerra, J.; Nguyen, D.-T.; Gopalakrishnan, V.-N.; Do, T.-O. Plasmonic Au nanoparticles incorporated in the zeolitic imidazolate framework (ZIF-67) for the efficient sunlight-driven photoreduction of CO_2. *ACS Appl. Energy Mater.* **2020**, *3*, 7659–7665. [CrossRef]
28. Lertthanaphol, N.; Prawiset, N.; Soontornapaluk, P.; Kitjanukit, N.; Neamsung, W.; Pienutsa, N.; Chusri, K.; Sornsuchat, T.; Chanthara, P.; Phadungbut, P.; et al. Soft template-assisted copper-doped sodium dititanate nanosheet/graphene oxide heterostructure for photoreduction of carbon dioxide to liquid fuels. *RSC Adv.* **2022**, *12*, 24362–24373. [CrossRef]
29. Wang, G.; He, C.-T.; Huang, R.; Mao, J.; Wang, D.; Li, Y. Photoinduction of Cu single atoms decorated on UiO-66-NH_2 for enhanced photocatalytic reduction of CO_2 to liquid fuels. *J. Am. Chem. Soc.* **2020**, *142*, 19339–19345. [CrossRef]
30. Maimaitizi, H.; Abulizi, A.; Kadeer, K.; Talifu, D.; Tursun, Y. In situ synthesis of Pt and N co-doped hollow hierarchical BiOCl microsphere as an efficient photocatalyst for organic pollutant degradation and photocatalytic CO_2 reduction. *Appl. Surf. Sci.* **2020**, *502*, 144083. [CrossRef]
31. Ma, M.; Huang, Z.; Doronkin, D.-E.; Fa, W.; Rao, Z.; Zou, Y.; Wang, R.; Zhong, Y.; Cao, Y.; Zhang, R.; et al. Ultrahigh surface density of Co-N_2C single-atom-sites for boosting photocatalytic CO_2 reduction to methanol. *Appl. Catal. B Environ.* **2022**, *300*, 120695. [CrossRef]
32. Wu, J.; Xie, Y.; Ling, Y.; Si, J.; Li, X.; Wang, J.; Ye, H.; Zhao, J.; Li, S.; Zhao, Q.; et al. One-step synthesis and Gd^{3+} decoration of BiOBr microspheres consisting of nanosheets toward improving photocatalytic reduction of CO_2 into hydrocarbon fuel. *Chem. Eng. J.* **2020**, *400*, 125944. [CrossRef]
33. Ribeiro, C.-S.; Lansarin, M.-A. Enhanced photocatalytic activity of Bi_2WO_6 with PVP addition for CO_2 reduction into ethanol under visible light. *Environ. Sci. Pollut. Res.* **2021**, *28*, 23667–23674. [CrossRef] [PubMed]
34. Seeharaj, P.; Kongmun, P.; Paiplod, P.; Prakobmit, S.; Sriwong, C.; Kim-Lohsoontorn, P.; Vittayakorn, N. Ultrasonically-assisted surface modified TiO_2/rGO/CeO_2 heterojunction photocatalysts for conversion of CO_2 to methanol and ethanol. *Ultrason. Sonochem.* **2019**, *58*, 104657. [CrossRef]
35. Ribeiro, S.-C.; Lansarin, A.-M. Facile solvo-hydrothermal synthesis of Bi_2MoO_6 for the photocatalytic reduction of CO_2 into ethanol in water under visible light. React. *Kinet. Mech. Catal.* **2019**, *127*, 1059–1071. [CrossRef]
36. Vu, N.-N.; Nguyen, C.-C.; Kaliaguine, S.; Do, T.-D. Reduced Cu/Pt–$HCa_2Ta_3O_{10}$ Perovskite Nanosheets for Sunlight-Driven Conversion of CO_2 into Valuable Fuels. *Adv. Sust. Syst.* **2017**, *1*, 1700048. [CrossRef]